Journal of
Materials Chemistry C

ROYAL SOCIETY
OF CHEMISTRY

PAPER

View Article Online
View Journal | View Issue

Check for updates

Cite this: *J. Mater. Chem. C*, 2025, **13**, 15628

Deep-red TADF dendronized polymer for efficient non-doped solution-processed OLEDs†

Chensen Li, ‡*[a] Xiansheng Li,‡[a] Xin Luo,[a] Bo Xu, *[a] Martin R. Bryce, *[b] Zhongjie Ren *[c] and Shouke Yan [cd]

Significant progress has been made in red thermally activated delayed fluorescence (TADF) emitters, but efficient solution-processable deep-red TADF polymers and their non-doped organic light-emitting diodes (OLEDs) are rarely reported. A novel deep-red TADF dendronized polymer **PNAI-AcCz** was synthesized to address this issue. First, the acridan donor was encapsulated by 3,6-di-*tert*-butylcarbazole *via* conjugated linkage to raise the highest occupied molecular orbital (HOMO) energy level and decrease aggregation caused quenching; then a non-conjugated carbazole connects the 1,8-naphthalimide acceptor to increase the solubility; finally, a linear dendronized copolymer was obtained by homopolymerization with an alkyl backbone as the main chains. The highly twisted donor–acceptor architecture leads to a small singlet–triplet energy gap of 0.015 eV, high photoluminescence quantum yield of 15%, and short delayed fluorescence lifetime of 4.20 μs. The non-doped solution-processed OLED based on **PNAI-AcCz** achieved a high EQE of 2.6% with a deep-red emission peak at 659 nm, which is the highest EQE value reported to date in the non-doped solution-processed deep-red TADF OLEDs.

Received 5th June 2025,
Accepted 24th June 2025

DOI: 10.1039/d5tc02176f

rsc.li/materials-c

Introduction

Deep-red organic light-emitting diodes (OLEDs),[1,2] characterized by emission wavelengths beyond 650 nm, are indispensable components in high-fidelity displays and biomedical sensing due to their unique spectral compatibility with human vision and tissue penetration capabilities. However, achieving efficient deep-red electroluminescence remains a formidable challenge: conventional fluorescent emitters suffer from low exciton utilization ($<25\%$),[1] while phosphorescent complexes reliant on rare metals (*e.g.*, iridium or platinum)[3,4] face prohibitive costs and environmental concerns. All-organic thermally activated delayed fluorescence (TADF) materials,[5,6] which enable 100% exciton harvesting through reverse intersystem crossing (RISC), have emerged as a sustainable alternative. Nevertheless, existing small-molecule red TADF[7–9] molecules typically face serious aggregation-caused quenching (ACQ) issues and predominantly require complex host–guest systems with critical limitations. This system not only triggers a significant blue shift in the spectra through the doped host but also demands precise control of doping concentrations, complicating large-scale manufacturing.[10] Additionally, energy transfer between host and guest materials often induces undesired blueshifts in the emission spectrum, especially under high driving voltages, thereby deviating from the deep-red wavelength.[11] Therefore, the development of non-doped deep-red TADF systems has been hindered by trade-offs among deep-red emission and aggregation-induced efficiency losses. This gap underscores the urgent need for innovative molecular designs that transcend current material limitations.[12]

Compared with vacuum-deposited deep-red OLEDs, solution-processable deep-red OLEDs offer key advantages, such as low-cost fabrication *via* inkjet printing or spin-coating, compatibility with flexible substrates for lightweight electronics, and scalability for large-area displays.[13–15] However, their efficiency currently lags behind vacuum-deposited devices. Design rules for deep-red TADF molecules require balancing small singlet–triplet gaps ($\Delta E_{ST} < 0.2$ eV), efficient reverse intersystem crossing (RISC), and solution processability. The common design strategies

---

[a] *Key Laboratory for Soft Chemistry and Functional Materials of Ministry of Education, School of Chemistry and Chemical Engineering, Nanjing University of Science and Technology, Nanjing, Jiangsu, 210094, China. E-mail: chensenli@njust.edu.cn, boxu@njust.edu.cn*

[b] *Chemistry Department, Durham University, South Road, Durham, DH1 3LE, UK. E-mail: m.r.bryce@durham.ac.uk*

[c] *State Key Laboratory of Chemical Resource Engineering, Beijing Advanced Innovation Centre for Soft Matter Science and Engineering, Beijing University of Chemical Technology, Beijing 100029, China. E-mail: renzj@mail.buct.edu.cn*

[d] *Key Laboratory of Rubber-Plastics, Ministry of Education, Qingdao University of Science & Technology, Qingdao, 266042, P. R. China*

† Electronic supplementary information (ESI) available: Synthetic pathways, structural analyses, photophysical investigations, complemented by additional experimental details, materials, and method descriptions. See DOI: https://doi.org/10.1039/d5tc02176f

‡ C. L. and X. L. contributed equally.

include: (1) strong donor–acceptor systems with extended π-conjugation or intramolecular charge transfer (ICT) to achieve deep-red emission;[16] (2) enhanced spin–orbit coupling (SOC) *via* heteroatoms to promote ^{3}CT-^{3}LE mixing;[17] (3) rigidification and aggregation-induced emission (AIE) property to suppress non-radiative decay and oxygen quenching;[18] (4) alkyl-chain modification for solution processability and film formation.[19] TADF polymers[20] are promising for efficient non-doped solution-processing of deep-red OLEDs. While conjugated polymers[21] can enhance solution processability, their rigid backbones often lead to strong intermolecular interactions, resulting in redshifted emission but compromised photoluminescence quantum yields (PLQYs). Furthermore, achieving a small ΔE_{ST} in deep-red emitters is intrinsically difficult due to the extended π-conjugation required for long-wavelength emission. Achieving high-efficiency deep-red TADF emitters is also hindered as non-radiative transition processes increase sharply with decreasing bandgaps, in line with the energy-gap law.[22] These limitations underscore the urgent need for innovative polymer designs that integrate long wavelength emission, efficient TADF characteristics, and compatibility with non-doped solution processing.

To address these challenges, we exploit a dendronized polymer strategy[19,20] that synergistically optimizes molecular orbital energy levels, solubility, and exciton utilization. Specifically, we designed **PNAI-AcCz**, a novel deep-red TADF polymer with the following structural features. (i) A twisted donor–acceptor (D–A) architecture. (ii) By encapsulating an acridan donor with sterically hindered 3,6-di-*tert*-butylcarbazole *via* conjugated linkages, the highest occupied molecular orbital (HOMO) energy level is elevated while suppressing ACQ. (iii) Enhanced solubility is achieved by introduction of non-conjugated carbazole spacers linked to a strong 1,8-naphthalimide (NAI)[23,24] acceptor which enables both efficient charge transfer and improved solubility. (iv) A linear dendronized topology: homo-polymerization with an alkyl backbone ensures processability while maintaining a small ΔE_{ST} (< 0.015 eV) through controlled conjugation length. This molecular engineering approach yields a deep-red TADF emitter with a photoluminescence peak at 659 nm, a high PLQY of 15%, and a remarkably short delayed fluorescence lifetime of 4.20 μs. When applied in non-doped solution-processed OLEDs, the **PNAI-AcCz**-based device achieves a record external quantum efficiency (EQE) of 2.6%. This work demonstrates a practical approach to efficient solution-processed OLEDs and provides fundamental design insights for deep-red TADF polymers.

Chensen Li

Dr Chensen Li obtained his PhD from Beijing University of Chemical Technology in 2020 under the supervision of Prof. Shouke Yan, with a joint training period at Durham University (UK) in Prof. Martin Bryce's group. He conducted postdoctoral research (2021–2025) in Prof. Ben Zhong Tang's group at The Hong Kong University of Science and Technology before joining Nanjing University of Science and Technology as an associate professor in 2025. His research focuses on organic optoelectronic materials and devices. He has published over 10 first author papers in high-impact journals including Nat. Rev. Mater., J. Am. Chem. Soc., Angew. Chem. Int. Ed., Chem, and Nano Energy, with total citations exceeding 2000.

Results and discussion

Synthesis and characterization

The synthetic routes to **PNAI-AcCz** are described in the ESI† (Scheme S1). **PNAI-AcCz** was obtained by free radical polymerization of the corresponding vinyl-substituted monomer. The structures of the target material, and of the synthetic intermediates, were established by ^{1}H and ^{13}C-NMR spectroscopy, mass spectrometry and elemental analysis (Fig. S1–S15, ESI†). The molecular weight (M_n) of **PNAI-AcCz** was 13.0 kDa and the polydispersity index (PDI) was 1.46 by gel permeation chromatography (GPC) (Fig. S16, ESI†). The target material has good solubility in common organic solvents such as chloroform, toluene, dichloromethane, chlorobenzene and tetrahydrofuran. **PNAI-AcCz** has a thermal decomposition temperature (T_d) with 5% weight loss range of 433 °C by thermal gravimetric analysis (TGA), and its glass transition temperature (T_g) is 103 °C, indicating good thermal stability under OLED fabrication conditions (Fig. S17, ESI†). The cyclic voltammetry (CV) in CH_3CN solution shows the polymer undergoes quasi-reversible oxidation at 0.63 V (Fig. S18, ESI†), attributed to the acridan donor and carbazole units (Fig. 1).[25]

Theoretical calculation

The molecular simulation of **PNAI-AcCz** by density functional theory (DFT) B3LYP/6-31G (d) by Gaussian 16 (Fig. 2) shows the minimum energy molecular conformation and HOMO and lowest unoccupied molecular orbital (LUMO) distributions. Notable conformational features of **PNAI-AcCz** are a dihedral angle of 88.8° between the planes of the acridan donor and the NAI acceptor, and a dihedral angle of 56.9° between the acridan donor and the attached carbazole dendrons. The conjugation of the 3,6-di-*tert*-butylcarbazole units with acridan enhances the electron donating ability, and therefore the HOMO distribution is mainly on these three subunits, while the LUMO is mainly distributed on the NAI acceptor. The pronounced spatial decoupling between HOMO and LUMO achieves significant minimization of ΔE_{ST} (0.008 eV), which facilitates efficient RISC and consequently endows the polymer with remarkable TADF characteristics. To explore the excited state properties, the natural transition orbital (NTO) analyses were performed to investigate the nature of the excited states by Multiwfn.[26] The

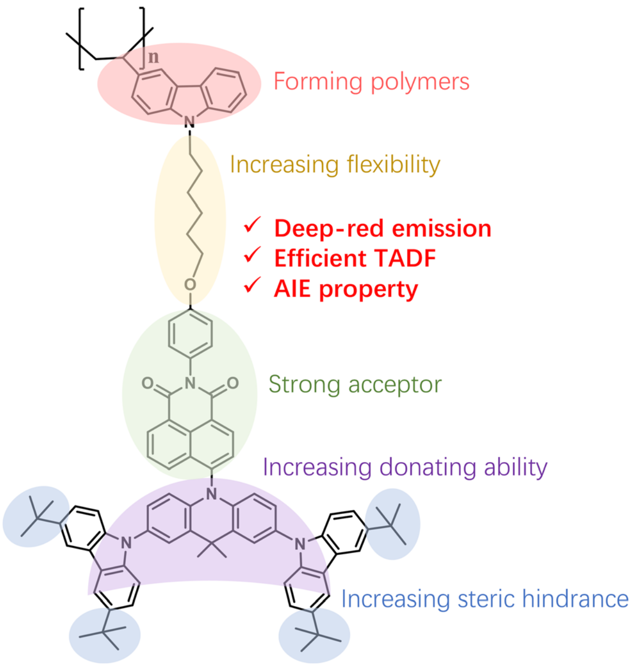

Fig. 1 Design strategies and structure for the deep-red TADF dendronized polymer **PNAI-AcCz**.

hole and electron of the $S_1(^1CT)$ and $T_1(^3CT)$ states of the polymer are separately distributed on the acridan donor and NAI acceptor, and the localized hole and electron of $T_2(^3LE)$ excited state of the dendronized polymer is distributed in the NAI acceptor. Due to the similar electron configurations between $S_1(^1CT)$ and $T_1(^3CT)$, the spin–orbit coupling (SOC) constant between the two states exhibits a small value (0.077 cm^{-1}), which is unfavourable for efficient RISC to occur. In contrast, the narrow T_2–T_1 energy gap (0.13 eV) facilitates rapid internal conversion (IC), while the pronounced spin–orbit coupling (SOC) between ^1CT and ^3LE (0.58 cm^{-1}) promotes efficient an RISC process, thereby enabling accelerated exciton harvesting.

Photophysical properties

To investigate the photoluminescence (PL) properties of **PNAI-AcCz**, the UV-Vis absorption and fluorescence spectra of **PNAI-AcCz** were recorded (Fig. 3a and b, Table 1). The polymer exhibits two types of absorption bands: the bands at 330 and 350 nm are mainly attributed to the π–π^* transition of carbazole units,[19] and the bands at 400–550 nm are mainly attributed to intramolecular charge transfer (ICT) between the electron donor/acceptor units,[20] which implies strong charge transfer in **PNAI-AcCz**. The fluorescence spectra of dilute toluene solution show a deep-red emission peak at 666 nm with charge transfer characteristics and a near-ultraviolet fluorescence band assigned to the carbazole unit at 370–390 nm. This unit is separated from the TADF emitter by the non-conjugated hexyloxy spacer, and the carbazole appears not to be involved in ICT in dilute solution. PNAI-AcCz exhibits distinct positive solvatochromism: emission redshifts from 607 nm (hexane, $\varepsilon = 1.9$) to 666 nm (toluene, $\varepsilon = 2.4$) and 741 nm (chloroform, $\varepsilon = 4.8$) with increasing solvent polarity (Fig. 3b). This confirms typical polarity-dependent emission and strong charge-transfer character. To investigate the aggregated optical properties, PL measurements were performed in solvent–nonsolvent systems. **PNAI-AcCz** exhibits weak blue/red emissions in THF solution, but the PL intensity increases with rising water content.

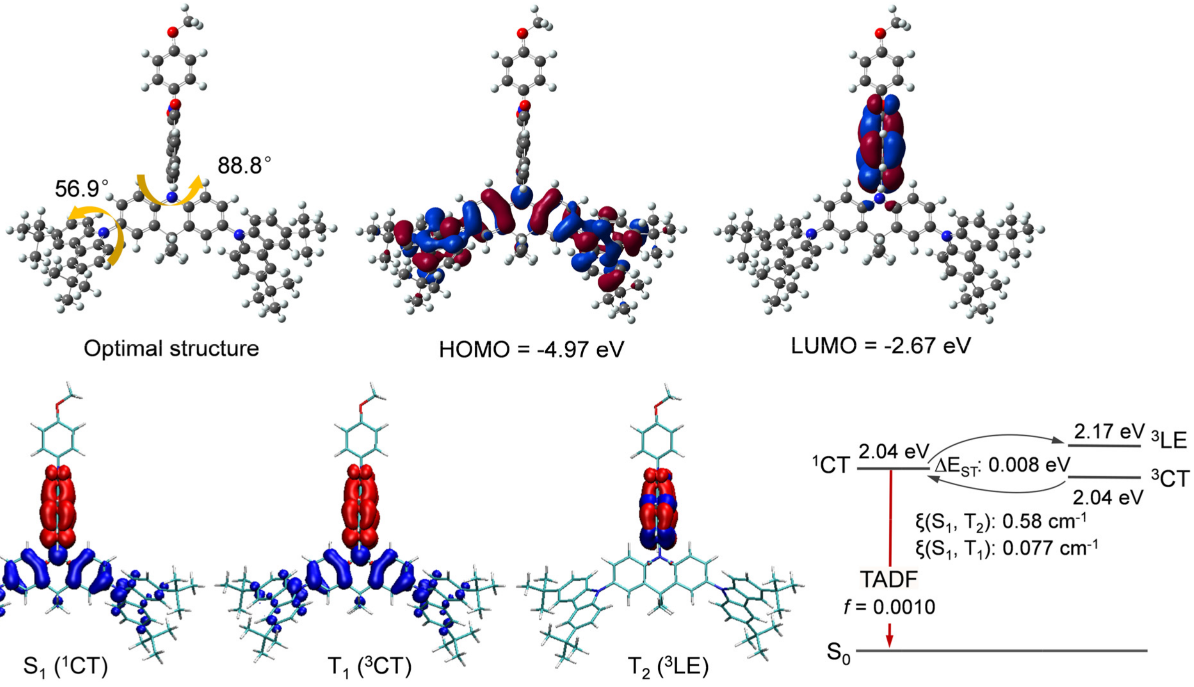

Fig. 2 Molecular structures, frontier orbital distributions and natural transition orbital (NTO) analysis of **PNAI-AcCz**.

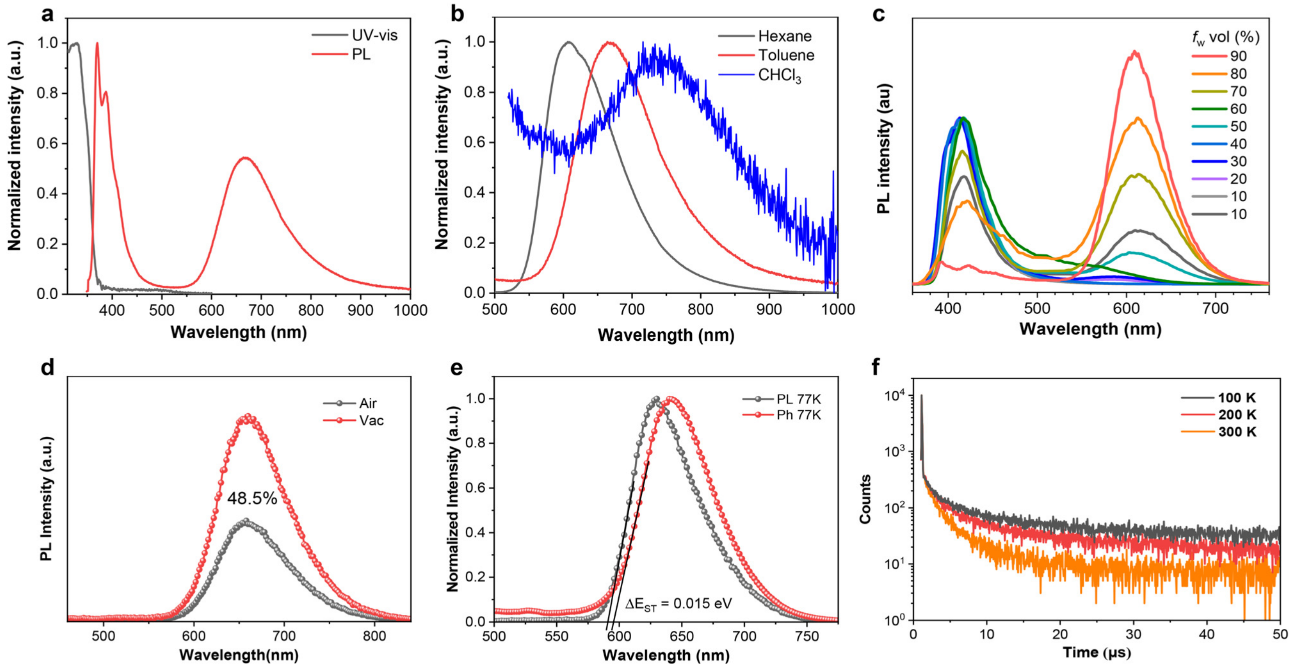

Fig. 3 PL behaviors of **PNAI-AcCz**. (a) UV-vis absorption and PL spectra in toluene solution. (b) PL spectra in hexane, toluene and chloroform solution. (c) PL spectra in water/THF mixtures with different fractions of water. (d) PL spectra in degassed and oxygenated films. (e) Fluorescence and phosphorescent spectra in neat films collected at 77 K. (f) PL transient decays in neat films at different temperatures.

Table 1 Photophysical properties of **PNAI-AcCz**

Emitter	λ_{ex} (nm)[a]	λ_{em} (nm)[a]	HOMO/LUMO (eV)[b]	ΔE_{ST} (eV)[c]	PLQY (%)[d]	$\tau_{\text{PF}}/\tau_{\text{DF}}$ (ns/μs)[e]	k_r (s^{-1})[f]	k_{nr} (s^{-1})[g]	k_{RISC} (s^{-1})[h]
PNAI-AcCz	330, 490	370, 666	−5.43/−3.36	0.015	15	49/4.20	3.18×10^4	2.02×10^5	3.25×10^5

[a] The absorption and emission peak of PL spectra measured in dilute toluene at room temperature. [b] Calculated according to the equation $E_{\text{HOMO}} = -(E_{(\text{onset, ox } vs. \text{ Fc+/Fc})} + 4.8)$ and LUMO = HOMO + E_g. The optical energy gap (E_g) deduced from the absorption onset in toluene. [c] Singlet and triplet energies were determined from the onset wavelength of fluorescence and phosphorescence at 77 K in neat films. [d] Absolute PL quantum yield in neat films, respectively, determined by a calibrated integrating sphere in nitrogen atmosphere. [e] The lifetime of prompt and delayed fluorescence component. [f] The rate constant of radiative transition calculated from $k_r = \Phi_{\text{DF}}/\tau_{\text{DF}}$. [g] The nonradiative decay rate of triplet exciton calculated from $k_{\text{nr}} = (1 - \Phi_{\text{DF}})/\tau_{\text{DF}}$. [h] The rate constant of reverse intersystem crossing calculated from $k_{\text{RISC}} = \Phi_{\text{PL}}/(\tau_{\text{DF}} \times (1 - \Phi_{\text{DF}}))$.

Notably, a sharp enhancement of the red emission peak is observed at a 10 : 90 (v/v) THF/water ratio, clearly demonstrating the AIE characteristics[27–29] (Fig. 3c). The twisted molecular conformation of red TADF units facilitates loose packing with weak intermolecular interactions, allowing for easy molecular rotation and vibration in dilute solutions. However, in the aggregated state, these intramolecular motions become effectively restricted, thereby suppressing nonradiative decay pathways of the excited state. Consequently, the red emission intensity progressively strengthens with increasing water fraction.

The fluorescence spectra of pure neat films (Fig. 3d) show a different profile from those in solution, since emission from the carbazole units at 370–390 nm is missing, indicating strong charge transfer from carbazole to TADF emitter in the aggregate state. In addition, the ratio between the delayed and prompt fluorescence (DF and PF) was determined from the integration of the steady-state spectra obtained in degassed and aerated conditions; this is because triplets which are involved in DF are quenched by oxygen. The corresponding spectra of **PNAI-AcCz** in neat films are shown in Fig. 3d. Moreover, the PLQY of **PNAI-AcCz** in neat films is measured to be 9% under ambient conditions and 15% (Table 1) under nitrogen atmosphere. Fig. S19 (ESI†) displays the PL lifetime decay curves of the polymer film under oxygenated and oxygen-free conditions, confirming its TADF behaviour. In the absence of oxygen, **PNAI-AcCz** exhibits a biexponential decay, with prompt fluorescence (nanosecond scale) and delayed fluorescence (microsecond scale). Notably, it still shows a biexponential decay even in the presence of oxygen, indicating retained TADF activity. This oxygen-resistant TADF can be attributed to the shielding effect provided by the entangled polymer chains.[19,20] The flexible alkyl linker enables the carbazole dendrons to partially encapsulate the central TADF core, suppressing triplet-state quenching by oxygen. Moreover, the fluorescence and phosphorescence spectra of the sample in neat film at 77 K (Fig. 3d) reveal a ΔE_{ST} of 0.015 eV (Table 1), calculated from the onset energies of the respective emission bands. This small value

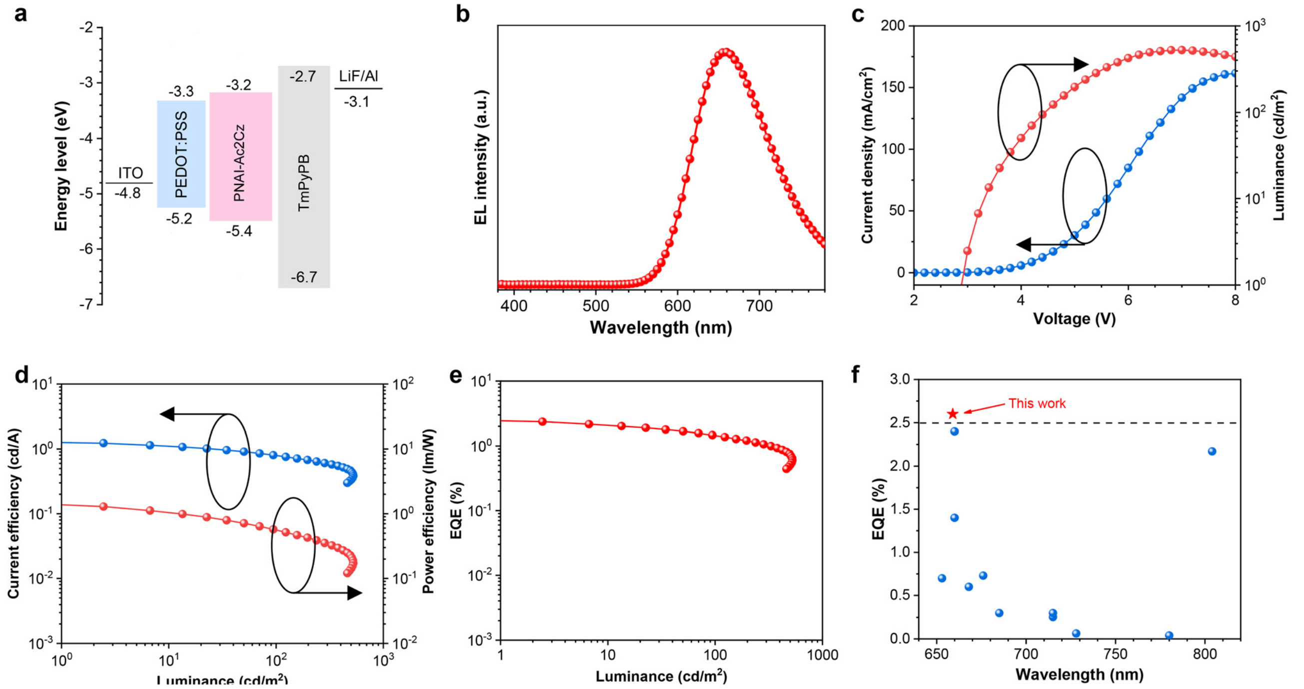

Fig. 4 (a) Energy-level diagrams and structures of OLED device. (b) Normalized EL spectra at 5 V. (c) Current density–voltage–luminance curves. (d) Current efficiency–current density–power efficiency curves. (e) External quantum efficiency *versus* luminance curves. (f) EL efficiency statistics based on solution-processed deep-red TADF-OLEDs.

indicates that the dendronized polymer should readily undergo RISC and be TADF-active. The delayed fluorescence lifetime of **PNAI-AcCz** is 4.69, 4.40 and 4.20 μs at 100, 200 and 300 K, respectively, and the DF ratios are enhanced from 81.4%, 87.9% to 89.0% with increasing temperatures (Fig. 3f and Table 1). The transient PL directly resolves the temporal decay profile, providing unambiguous DF weight. The dendronized polymer shows the shortest DF lifetime and highest DF ratio at 300 K, suggesting that higher temperature is more conducive to the effective RISC process. Indeed, the RISC rate (k_{RISC}) was calculated to be 3.25×10^5 s^{-1} for **PNAI-AcCz** (Table 1).

OLED Performance

To investigate electroluminescent (EL) properties of **PNAI-AcCz**, non-doped OLEDs were fabricated by solution processing with a configuration of device (Fig. 4a): ITO/poly(3,4-ethylenedioxythiophene): poly(styrenesulfonate) (PEDOT:PSS) (40 nm)/**PNAI-AcCz** (EML) (40 nm)/1,3,5-tri(*m*-pyrid-3-yl-phenyl)benzene (TmPyPB) (42 nm)/LiF (1 nm)/Al (100 nm). The current density–voltage–luminance (*J*–*V*–*L*) characteristics, the EQEs *versus* luminance curves, and the EL spectra for all these devices are shown in Fig. 4b–e. The devices exhibit deep-red EL emission with $\lambda_{\max}$ 659 nm (CIE$_{x,y}$: 0.67, 0.33), which is slightly blue shifted comparing to its PL spectrum in neat film. The device achieves a low turn-on voltage of 3.0 V due to the good matching of energy levels of the component layers. The device achieves a maximum luminance of 525 cd m^{-2}, a maximum current efficiency (CE) of 1.31 cd A^{-1}, and a maximum power efficiency (PE) of 1.44 lm W^{-1}. In addition, a maximum EQE of 2.60% was observed, which is the highest efficiency for solution-processed deep-red TADF-OLEDs (Fig. 4f and Table S1, ESI†). The theoretical value of the exciton utilization efficiency (EUE) was calculated by using the following equation:

$$\mathrm{EQE} = \gamma \eta_{\mathrm{out}} \Phi_{\mathrm{PL}} \times \mathrm{EUE}$$

where γ is the charge balance factor, η_{out} is the light out-coupling efficiency, Φ_{PL} is the PLQY. Given the perfect charge balance ($\gamma = 1$) and light out-coupling efficiency (η_{out}) of 20% in the devices. A high EUE of 86.7% in the EL process demonstrates that the triplet excitons have been effectively utilized. Moreover, the EQE remains at 1.46% at 100 cd m^{-2}, demonstrating low efficiency roll-off. These excellent EL performances can be attributed to the small ΔE_{ST}, high PLQY, short lifetime, suppressed exciton quenching and AIE property of the dendronized polymer.

Conclusions

In summary, a novel deep-red TADF polymer was successfully designed and synthesized through a strategic combination of conjugated and non-conjugated carbazole linkages. The polymer architecture integrates a half-dendronized acridan-1,8-naphthalimide TADF core with a partially encapsulated acridan unit, followed by the introduction of a flexible alkyl polymer backbone to form the linear dendronized polymer **PNAI-AcCz**. This unique design endows the material with exceptional TADF characteristics, achieved through two key mechanisms: (1) AIE properties, which effectively suppress concentration quenching; (2) dendronization, which enhances the stability of triplet excitons against oxygen quenching. The resulting host-free **PNAI-AcCz**-based OLED exhibits an EQE_{max} of 2.6% with an EL peak at 659 nm, representing the highest reported efficiency for solution-processed deep-red TADF-OLEDs to date. These findings not only demonstrate a promising approach for developing high-performance deep-red TADF macromolecules but also pave the way for more efficient solution-processable deep-red OLED devices.

Author contributions

Chensen Li conceptual design, investigation, synthesis of compounds, processing of test data, writing – original draft. Xiansheng Li: investigation, visualization and validation. Xin Luo: investigation. Bo Xu, Martin R. Bryce, and Zhongjie Ren: method inquiry, project administration, funding acquisition, writing-review, and editing. Shouke Yan: supervision and resources.

Conflicts of interest

There are no conflicts to declare.

Data availability

The data that support the findings of this study are available in the ESI† of this article.

Acknowledgements

Zhongjie Ren acknowledges National Natural Science Foundation of China (No. 52273164) for funding. Martin R. Bryce acknowledges the EPSRC for funding under grant numbers EP/L02621X/1. Bo Xu acknowledges Natural Science Foundation of Jiangsu Province (BK20240083), National Natural Science Foundation of China (W2412114, 22279059). Chensen Li acknowledges the Fundamental Research Funds for the Central Universities (No. 30925010203).

Notes and references

1 C.-T. Chen, *Chem. Mater.*, 2004, **16**, 4389–4400.
2 Y. Sun, W. Sun, D. Zhang, J. Yin, M. Mao and L. Zhou, *J. Phys. Chem. C*, 2023, **127**, 19378–19385.
3 B. Jiang, Y. Gu, J. Qin, X. Ning, S. Gong, G. Xie and C. Yang, *J. Mater. Chem. C*, 2016, **4**, 3492–3498.
4 Z. Wen, Y. Xu, X.-F. Song, J. Miao, Y. Zhang, K. Li and C. Yang, *Adv. Opt. Mater.*, 2023, **11**, 2300201.
5 H. Uoyama, K. Goushi, K. Shizu, H. Nomura and C. Adachi, *Nature*, 2012, **492**, 234–238.
6 Y. Liu, C. Li, Z. Ren, S. Yan and M. R. Bryce, *Nat. Rev. Mater.*, 2018, **3**, 18020.
7 L. Hua, Y. Liu, H. Zhao, S. Chen, Y. Zhang, S. Yan and Z. Ren, *Adv. Funct. Mater.*, 2023, **33**, 2303384.
8 L. Hua, Y. Liu, B. Liu, Z. Zhao, L. Zhang, S. Yan and Z. Ren, *Nat. Commun.*, 2022, **13**, 7828.
9 M. Li, L. Hua, J. Zhao, Y. Liu, S. Yan and Z. Ren, *Angew. Chem., Int. Ed.*, 2025, **64**, e202501179.
10 M. Zhao, M. Li, W. Li, S. Du, Z. Chen, M. Luo, Y. Qiu, X. Lu, S. Yang, Z. Wang, J. Zhang, S. J. Su and Z. Ge, *Angew. Chem., Int. Ed.*, 2022, **61**, e202210687.
11 J. Xu, J. Xue, Y. Dai, J. Zhang, J. Ren, C. Yao, S. Li, Q. Meng, X. Wen, H. Shao and J. Qiao, *Aggregate*, 2024, **5**, e634.
12 H. Wang, S. Lin, J. X. Chen, X. Y. Hao, X. C. Fan, Y. Z. Shi, J. Yu, X. K. Chen, K. Wang and X. H. Zhang, *Adv. Funct. Mater.*, 2025, **35**, 2420489.
13 C. Li, R. S. Nobuyasu, Y. Wang, F. B. Dias, Z. Ren, M. R. Bryce and S. Yan, *Adv. Opt. Mater.*, 2017, **5**, 1700435.
14 C. Li, Y. Xu, Y. Liu, Z. Ren, Y. Ma and S. Yan, *Nano Energy*, 2019, **65**, 104057.
15 T. Wang, Y. Cheng and C. Yang, *Prog. Polym. Sci.*, 2024, **158**, 101892.
16 Y. Yu, H. Xing, D. Liu, M. Zhao, H. H. Sung, I. D. Williams, J. W. Y. Lam, G. Xie, Z. Zhao and B. Z. Tang, *Angew. Chem., Int. Ed.*, 2022, **61**, 202204279.
17 F. B. Dias, J. Santos, D. R. Graves, P. Data, R. S. Nobuyasu, M. A. Fox, A. S. Batsanov, T. Palmeira, M. N. Berberan-Santos, M. R. Bryce and A. P. Monkman, *Adv. Sci.*, 2016, **3**, 1600080.
18 Z. Zhao, H. Zhang, J. W. Y. Lam and B. Z. Tang, *Angew. Chem., Int. Ed.*, 2020, **59**, 9888–9907.
19 C. Li, A. K. Harrison, Y. Liu, Z. Zhao, C. Zeng, F. B. Dias, Z. Ren, S. Yan and M. R. Bryce, *Angew. Chem., Int. Ed.*, 2022, **61**, e202115140.
20 C. Li, A. K. Harrison, Y. Liu, Z. Zhao, F. B. Dias, C. Zeng, S. Yan, M. R. Bryce and Z. Ren, *Chem. Eng. J.*, 2022, **435**, 134924.
21 Y. Liu, Y. Wang, C. Li, Z. Ren, D. Ma and S. Yan, *Macromolecules*, 2018, **51**, 4615–4623.
22 R. Englman and J. Jortner, *Mol. Phys.*, 1970, **18**, 145–164.
23 W. Zeng, H. Y. Lai, W. K. Lee, M. Jiao, Y. J. Shiu, C. Zhong, S. Gong, T. Zhou, G. Xie, M. Sarma, K. T. Wong, C. C. Wu and C. Yang, *Adv. Mater.*, 2017, **30**, 201704961.
24 W. Zeng, T. Zhou, W. Ning, C. Zhong, J. He, S. Gong, G. Xie and C. Yang, *Adv. Mater.*, 2019, **31**, 1901404.
25 K. Albrecht, K. Matsuoka, K. Fujita and K. Yamamoto, *Angew. Chem., Int. Ed.*, 2015, **54**, 5677–5682.
26 T. Lu and F. Chen, *J. Comput. Chem.*, 2012, **33**, 580–592.
27 K.-M. Liu, Y. Wang, F.-W. Xia, S. Feng, X.-Q. Yu and M.-Y. Wu, *Smart Mol.*, 2025, e20240060.
28 Y. Lu, H. Wang, Q. Li, Q. Liu, X. Zhang, Y. Jia, X. Cai, Z. Zhao, Y. Huan and B. Z. Tang, *Smart Mol.*, 2025, **3**, e20240011.
29 B. B. Chen, Y. T. Gao, M. L. Liu, D. W. Li, Q. Liu, Z. Zhao and B. Z. Tang, *Smart Mol.*, 2024, e20240053.